

ELEMENT ABUNDANCE ANALYSIS OF THE METAL-RICH STELLAR HALO AND HIGH-VELOCITY THICK DISK IN THE GALAXY

HAIFAN ZHU¹, CUIHUA DU², YEPENG YAN^{3,1}, JIANRONG SHI^{4,2}, JUN MA^{4,2}, HEIDI JO NEWBERG⁵

¹School of Physical Sciences, University of Chinese Academy of Sciences, Beijing 100049, China

²College of Astronomy and Space Sciences, University of Chinese Academy of Sciences, Beijing 100049, China; ducuihua@ucas.ac.cn

³Department of Astronomy, Beijing Normal University, Beijing 100875, China

⁴Key Laboratory of Optical Astronomy, National Astronomical Observatories, Chinese Academy of Sciences, Beijing 100012, China

⁵Department of Physics, Applied Physics and Astronomy, Rensselaer Polytechnic Institute, Troy, NY 12180, USA

Draft version February 1, 2022

ABSTRACT

Based on the second Gaia data release (DR2) and APOGEE (DR16) spectroscopic surveys, we defined two kinds of star sample: high-velocity thick disk (HVTD) with $v_\phi > 90\text{km/s}$ and metal-rich stellar halo (MRSH) with $v_\phi < 90\text{km/s}$. Due to high resolution spectra data from APOGEE (DR16), we can analyze accurately the element abundance distribution of HVTD and MRSH. These elements abundance constituted a multidimensional data space, and we introduced an algorithm method for processing multi-dimensional data to give the result of dimensionality reduction clustering. According to chemical properties analysis, we derived that some HVTD stars could origin from the thin disk, and some MRSH stars from dwarf galaxies, but those stars which have similar chemical abundance characteristics in both sample may form in-situ.

Subject headings: Galaxy:disk-Galaxy:halo-Galaxy:structure-Galaxy:kinematics-Stars:abundance

1. INTRODUCTION

The Halo and thick-disk are the basic components of the Galaxy, and the study to their kinematics and chemical abundance could provide important clues to the Galaxy's formation and evolution history. Recent studies (Carollo et al. 2007, 2010; Chen et al. 2011; Beers et al. 2012; Kinman et al. 2012) have shown that the Galactic halo comprises at least two stellar populations: inner-halo and outer halo. They have different kinematics, spatial distribution, and chemical composition (Carollo et al. 2007, 2012; Liu et al. 2018; Conroy et al. 2019; Bird et al. 2020). For example, the inner-halo is mainly distributed at distances up to 10–15 kpc from the Galactic center, and the mean metallicity of the inner-halo range from $[\text{Fe}/\text{H}] \sim -1.2$ dex to -1.7 dex. The outer-halo is mainly distributed at distances up to 15–20 kpc from the Galactic center, and the mean metallicity of the outer-halo range from $[\text{Fe}/\text{H}] \sim -1.9$ dex to -2.3 dex (e.g., Carollo et al. 2007; An et al. 2013, 2015; Zuo et al. 2017; Gu et al. 2015, 2016, 2019; Liu et al. 2018). Studies of the detailed chemical abundances and ages of halo stars have sought to place further constraints on the structure and formation of the Galactic halo (Naidu et al. 2020; Şahin & Bilir 2020). Many studies have shown that there are two chemically distinct stellar populations: an older, high- α , and a younger, low- α halo population, (e.g., Nissen & Schuster 2010, 2011; Bergemann et al. 2017; Hayes et al. 2018).

Particularly, after the second release of the Gaia (Gaia DR2), a significant number of works have revealed an even more complex but detailed picture of the Galactic halo. For example, Belokurov et al. (2018) showed the velocity ellipsoid becomes strongly anisotropic for the halo stars with $-1.7 < [\text{Fe}/\text{H}] < -1.0$ dex and local velocity distribution appears highly stretched in the radial direction, taking sausage-like shape, and they suggested that such orbital configurations could show that most of the inner halo stars should be dominated by stars accreted from an ancient massive merger event. This merger event referred as the Gaia-Sausage merger (e.g., Myeong et al. 2018, 2019; Deason et al. 2018; Lancaster et

al. 2019). Helmi et al. (2018) also demonstrated that the inner halo is dominated by debris from the merger of a dwarf galaxy 10 Gyr ago, and the dwarf galaxy referred as Gaia-Enceladus. Several other works also found new chemo-dynamical properties of the stellar halo, that were unknown before Gaia (e.g., Bonaca et al. 2017, 2020; Koppelman et al. 2019; Belokurov et al. 2019; Carollo et al. 2020; Yuan et al. 2020; Naidu et al. 2020; Yan et al. 2020). All these observation results imply that accreted stars from satellite galaxies have been suggested to be dominant inner halo component.

The Galactic disks contain a substantial fraction of their baryonic matter and angular momentum, and much of the evolutionary activity. The formation and evolution of disks are therefore very important (Kruit & Freeman 2011). The basic components of the Galactic disk are the thin-disk and thick-disk populations. The two components differ not only in their spatial distribution profiles but also in their kinematics, age and metallicity (Kruit & Freeman 2011; Ivezić et al. 2012; Xiang et al. 2015, 2017; Jing et al. 2016; Peng et al. 2018; Gandhi & Ness 2019; Han et al. 2020; Wu et al. 2021). Stars in the thick disk have the following characteristics compared to stars in the thin disk: older, kinematically hotter, metal-poor and enhanced in α -elements (e.g., Chiba & Beers 2000; Prochaska et al. 2000; Bensby et al. 2005). In addition, there is evidence for the additional presence of a metal-weak thick-disk (MWTD) population, rotationally supported, but extending to lower metallicity stars than the canonical thick disk (Morrison et al. 1990; Beers et al. 1995; Chiba & Beers 2000; Beers et al. 2002, 2014; Carollo et al. 2019; Yan et al. 2019). A key question now is whether these disk components can also be used to account for the chemical and kinematic measurements for the same stars. It turns out that, even with the new data collected, it is not easy to answer it.

Despite the past three decades of thick-disk studies, there is still no consensus on models for the formation and evolution of thick disk. The proposed simulations of thick disk formation can be generally divided into four groups: (a) accretion

from disrupted satellite galaxies (Abadi et al. 2003), (b) heating of the pre-existing thin disk due to minor mergers (Quinn et al. 1993), (c) in-situ triggered star formation during and after a gas-rich merger (Brook et al. 2004; Sales et al. 2009), (d) in-situ formation through radial migration (Sellwood & Binney 2002; Schönrich & Binney 2009a,b; Schönrich et al. 2011).

These currently discussed models of formation mechanisms for the thick disk predict various trends between the kinematics properties and the metallicity of disk stars. For example, some simulations of accretion from disrupted satellite galaxies can help to explain why there are so many old stars in circular orbits in the outskirts of galaxies and why the specific angular momentum and radial extent of the thick disk and thin disk are comparable although their ages are significantly different (Abadi et al. 2003). Furthermore, it provides an explanation for the dynamical and evolutionary distinction between the thick and thin disk components: the thick disk is mostly tidal debris from disrupted satellites, while the young thin disk consists mostly of stars formed in situ after the merging activity abates (Abadi et al. 2003). Some simulations of the thick disk formation via the accretion of satellites onto a pre-existing thin disk, showed that mergers with 10% – 20% mass of the host lead to the formation of thick disk (Villalobos & Helmi 2008). Using a different numerical implementation of the radial migration scenario, Schönrich, and Binney (Schönrich & Binney 2009a,b; Schönrich et al. 2011) showed radial migration plays an important role in the local Solar Neighborhood. Feuillet et al. (2019) studied the spatial changes in the $[\alpha/M]$ -age relation and $[M/H]$ -age relations of the Milky Way disk. The results are important constraints to Galactic simulations and chemical evolution models.

Kordopatis et al. (2020) used the chemo-dynamical method to give conclusions related to the formation of thick disks. They think the key to understanding the effect of the past accretions on the properties of the thick disk is the super-solar metallicity counter-rotating population. This population will provide us with a reliable sample of locally born retrograde stars in order to determine the exact time and weigh this merger (Grand et al. 2020).

Previous studies showed that most of halo stars are metal-poor. With the release of more survey data, some recent works have revealed a large number of metal-rich halo stars ($[\text{Fe}/\text{H}] > -1$ dex) (e.g., Nissen & Schuster 2010, 2011; Bonaca et al. 2017; Posti et al. 2018; Yan et al. 2020). Bonaca et al. (2017) use the first Gaia data release, the Radial Velocity Experiment (RAVE, Steinmetz et al. 2006) and the **Apache Point Observatory Galactic Evolution Experiment (APOGEE, Eisenstein et al. 2011)** to find that half of their halo sample is comprised of stars with $[\text{Fe}/\text{H}] > -1$ dex, and they proposed that metal-rich halo stars in the solar neighborhood actually formed in situ within the Galactic disk. It is possible that these stars have undergone radial migration that caused changes in their orbits. Yan et al. (2020) use the second Gaia data release (DR2), combined with the ongoing Large Sky Area Multi-Object Fiber Spectroscopic Telescope survey (LAMOST, also called Guoshoujing Telescope, Zhao et al. 2012) and APOGEE to show that there exist a high-velocity thick disk (HVTD) with $v_\phi > 90\text{km/s}$ and a metal-rich stellar halo (MRSH) with $v_\phi < 90\text{km/s}$ in the Galaxy. But the details of how high-velocity thick disk (HVTD) and metal-rich stellar halo (MRSH) form are not yet understood.

In this work, we use the APOGEE DR16 and Gaia DR2 data to obtain samples of HVTD and MRSH to study the de-

tailed abundance characteristics and give their possible origins. This paper is organized as follows: Sect.2 introduces the data selection and the method of distance determination, and give the division of HVTD and MRSH. Section 3 introduces the dimensionality reduction algorithm to present the element abundances analysis. In Sect.4, we analyze the results and compare them with some previous works, and give the possible origin of HVTD and MRSH. The summary and conclusions are given in Sect.5.

2. DATA

2.1. Data selection

The Apache Point Observatory Galactic Evolution Experiment (APOGEE), part of the Sloan Digital Sky Survey III, is a near-infrared (H-band; 1.51-1.70 μm) and high-resolution ($R \sim 22,500$) spectroscopic survey (Zasowski et al. 2013). In this study, we use the data from the sixteenth SDSS Data Release (DR16) and it provides accurate radial velocities, stellar parameters, and chemical abundances of about 26 chemical species for 430 000 stars covering both the northern and southern sky (Jönsson et al. 2020).

The second Gaia data release, Gaia DR2, provides high-precision positions, parallaxes, and proper motions for 1.3 billion sources brighter than magnitude $G \sim 21$ mag. More detailed information about Gaia can be found in Gaia Collaboration et al. (2018a,b). In this study, we get the high-resolution sample stars by cross-matching between the APOGEE DR16 and Gaia DR2 catalog. Stellar parameters (metallicity abundances, radial velocity, effective temperature, and surface gravity) are from the APOGEE DR16. Other necessary parameters (position, proper motion, and parallax) are from the Gaia DR2 catalog.

In order to obtain reliable results, we utilize the following selection criteria:

- parallax uncertainties $< 20\%$
- proper motion error < 0.2 mas/year
- radial velocity uncertainties < 10 km/s
- $[\text{Fe}/\text{H}]$ error < 0.2 dex
- $\text{S/N} > 20$ in the G-band

2.2. Distance and Velocity determination

Bailer-Jones (2015) discussed that the inversion of the parallax to obtain distance is not appropriate when the relative parallax error is more than 20 percent. We use the Bayesian approach (Bailer-Jones 2015; Astraatmadja & Bailer-Jones 2016a,b; Luri et al. 2018; Yan et al. 2019) to derive stellar distance.

According to Bayesian formula, the posterior probability can be written as follows:

$$P(\theta|\mathbf{x}) \propto P(\mathbf{x}|\theta)P(\theta) \\ = \exp\left[-\frac{1}{2}(\mathbf{x} - \mathbf{m}(\theta))^T \Sigma^{-1}(\mathbf{x} - \mathbf{m}(\theta))\right]P(\theta), \quad (1)$$

where $P(\mathbf{x}|\theta)$ is the likelihood, the symbol θ represent the parameter vectors which consists of heliocentric distance (d), tangential speed (v), and travel direction (ϕ , increasing anti-clockwise from north), written as

$$\theta = (d, v, \phi)^T. \quad (2)$$

\mathbf{x} is the observed data vector which consists of the parallax ($\overline{\omega}$), proper motion in R.A. (μ_{α^*}) and DEC. (μ_{δ}), written as

$$\mathbf{x} = (\overline{\omega}, \mu_{\alpha^*}, \mu_{\delta})^T. \quad (3)$$

The likelihood probability is a multidimensional Gaussian distribution centered on \mathbf{m} as we can see in the formula (1). Σ is covariance matrix

$$\Sigma = \begin{pmatrix} \sigma_{\overline{\omega}}^2 & \sigma_{\overline{\omega}}\sigma_{\mu_{\alpha^*}}\rho(\overline{\omega}, \mu_{\alpha^*}) & \sigma_{\overline{\omega}}\sigma_{\mu_{\delta}}\rho(\overline{\omega}, \mu_{\delta}) \\ \sigma_{\overline{\omega}}\sigma_{\mu_{\alpha^*}}\rho(\overline{\omega}, \mu_{\alpha^*}) & \sigma_{\mu_{\alpha^*}}^2 & \sigma_{\mu_{\alpha^*}}\sigma_{\mu_{\delta}}\rho(\mu_{\alpha^*}, \mu_{\delta}) \\ \sigma_{\overline{\omega}}\sigma_{\mu_{\delta}}\rho(\overline{\omega}, \mu_{\delta}) & \sigma_{\mu_{\alpha^*}}\sigma_{\mu_{\delta}}\rho(\mu_{\alpha^*}, \mu_{\delta}) & \sigma_{\mu_{\delta}}^2 \end{pmatrix}. \quad (4)$$

where $\rho(i, j)$ denotes the correlation coefficient between i and j and σ_k denotes the standard deviation of parameters k . \mathbf{m} represents a set of theoretical values predicted by our model, written as

$$\mathbf{m} = \left(\frac{10^3}{d}, c \frac{10^3 v \sin \phi}{d}, c \frac{10^3 v \cos \phi}{d} \right)^T \quad (5)$$

where $c = (\text{pc} \cdot \text{mas} \cdot \text{yr}^{-1}) / (4.74 \cdot \text{km s}^{-1})$.

$P(\theta)$ is the prior distribution given by Luri et al. (2018)

$$P(\theta) = P(d)P(v)P(\phi), \quad (6)$$

with

$$P(d) \propto \begin{cases} d^2 e^{-d/L(a,b)} & d > 0 \\ 0 & d \leq 0 \end{cases} \quad (7)$$

$$P(v) \propto \begin{cases} \left(\frac{v}{v_{\max}}\right)^{\alpha-1} \left(1 - \frac{v}{v_{\max}}\right)^{\beta-1} & \text{if } 0 \leq v \leq v_{\max} \\ 0 & \text{otherwise} \end{cases} \quad (8)$$

$$P(\phi) \propto \frac{1}{2\pi} \quad (9)$$

$L(a, b)$ is length scale of Galactic longitude- and latitude-dependent (Bailer-Jones 2015). Here we take $\alpha = 2$, $\beta = 3$, $v_{\max} = 750 \text{ km/s}$. Then we get the posterior distribution through the Markov chain Monte Carlo (MCMC) sampler EMCEE (Foreman-Mackey et al. 2013). We run each chain using 100 walkers and 100 steps, for a total of 10,000 random samples drawn from the posterior distribution. Finally, we adopt the data to calculate the kinematic parameters by using Astropy (Astropy Collaboration et al. 2013, 2018) and galpy (Bovy 2015). Astropy provides many functions to calculate the parameters and coordinate transformations. Galpy is a Python package for galactic dynamics and it supports orbit integration in various potentials.

When calculating with galpy, we choose the potential model from MWPotential2014 (Bovy 2015), the distance from the Sun to the Galactic center is 8.2 kpc and height above the plane is about 15 pc (Bland-Hawthorn & Gerhard 2016). When deriving velocity, we adopt $v_{\text{LSR}} = 232.8 \text{ km s}^{-1}$ (McMillan 2017). The velocity of the Sun with respect to the the local standard of rest (LSR) are $(U_{\odot}, V_{\odot}, W_{\odot}) = (10., 11., 7.) \text{ km s}^{-1}$ (Bland-Hawthorn & Gerhard 2016). Using the above, we can get the coordinate position, speed and orbit parameters.

2.3. Determination of HVTD and MRSH

In this study, we first get 4115 high velocity sample stars with $v_{\text{tot}} > 220 \text{ km s}^{-1}$. The sample stars distribution in the Toomre diagram is presented in Figure 1. In order to deter-

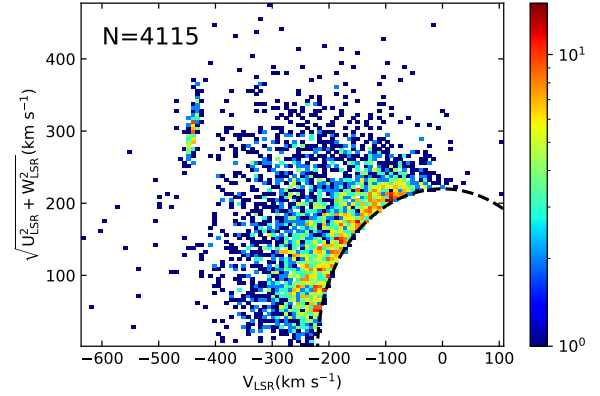


FIG. 1.— Toomre diagram of our high-velocity sample stars. The black dashed line represents the total spatial velocity $v_{\text{tot}} = 220 \text{ km s}^{-1}$ ($v_{\text{LSR}} = 232.8 \text{ km s}^{-1}$). Our high-velocity sample stars are defined as $v_{\text{tot}} > 220 \text{ km s}^{-1}$. The color bar represents the number of stars.

mine the HVTD component and the MRSH component, we also give the rotation velocity distribution of the sample stars with different metallicity selection in Figure 2. According to Yan et al. (2020), two-dimensional Gaussian fitting implied the existence of the HVTD and MRSH in the high-velocity sample, and they gave a definition of the division of the two components: HVTD with $v_{\phi} > 90 \text{ km s}^{-1}$ and $[\text{Fe}/\text{H}] > -1$ dex, MRSH with $v_{\phi} < 90 \text{ km s}^{-1}$ and $[\text{Fe}/\text{H}] > -1$ dex. Figure 3 gives the Toomre diagram. We can see that the distribution of HVTD and MRSH samples is quite different in the Toomre diagram. There is a small overlap near the dividing line.

The standard for division of two samples is derived from the characteristics of the bimodal distribution of the overall sample. It is not easy to obtain a clear boundary for the sample distribution. In this work, we directly adopted the previous division method.

The rotational velocity from 75 km s^{-1} to 125 km s^{-1} between the two peaks of the velocity distribution is suitable as division in Figure 2. Different dividing lines will affect the number of samples of MRSH and HVTD, but there are only 204 sample stars in this range for $[\text{Fe}/\text{H}] > -1$ dex and 176 sample stars for $[\text{Fe}/\text{H}] > -0.8$ dex. Furthermore, there are 65 stars in interval of v_{ϕ} [$75 \text{ km s}^{-1}, 90 \text{ km s}^{-1}$], 84 stars in interval [$90 \text{ km s}^{-1}, 110 \text{ km s}^{-1}$], 55 stars in interval [$110 \text{ km s}^{-1}, 125 \text{ km s}^{-1}$] with $[\text{Fe}/\text{H}] > -1$ dex. For $[\text{Fe}/\text{H}] > -0.8$ dex, the sample is even smaller. So even if changing the classification standard in this range, only classification of a very small sample of stars will be changed, and these changes will not have a substantial effect on the subsequent study.

2.4. Metallicity Distribution and Gradient

According to previous research, we use kinematic information to divide the sample stars into HVTD and MRSH. Figure 4 shows the metallicity distribution in the vertical distance $|z|$ of the two samples. We can notice that the distribution of HVTD is relatively concentrated, mainly in the range $< 3 \text{ kpc}$, and the distribution of MRSH is relatively uniform.

We use maximum likelihood estimation to derive the metallicity gradient in the $|z|$ direction. For a given sample with total number of stars N , the data points conform to the linear form $[\text{Fe}/\text{H}]_i = kz_i + b$. In this model, if position z_i , $[\text{Fe}/\text{H}]_i$ uncertainty σ_i , slope k (also $d[\text{Fe}/\text{H}]/dz$), and intercept b are

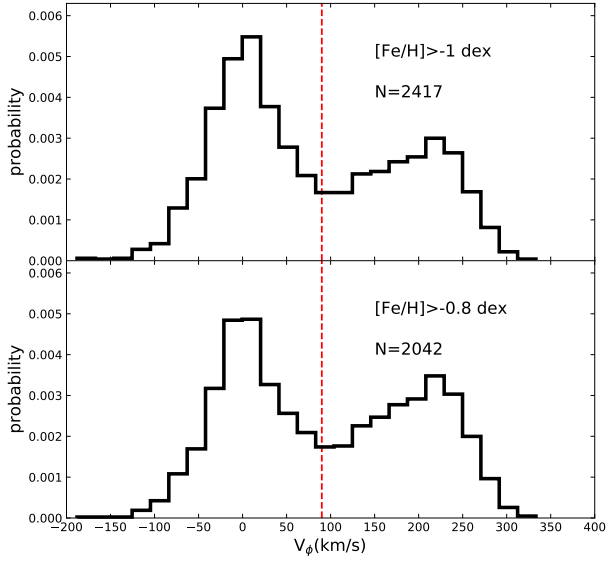


FIG. 2.— The rotational velocity distribution of high-velocity sample stars. Red dashed line is the division between HVTD and MRSH ($V_\phi = 90 \text{ km s}^{-1}$).

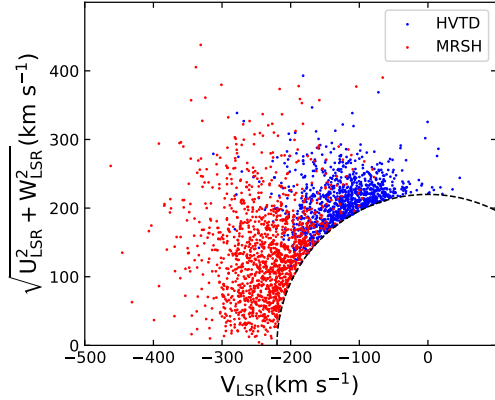


FIG. 3.— Toomre diagram of the HVTD (blue dots) sample and the MRSH (red dots) sample. The black dashed line represents the total spatial velocity $v_{\text{tot}} = 220 \text{ km s}^{-1}$. The two samples have a clear boundary and there are some overlapping parts at the boundary.

given, the distribution $P([\text{Fe}/\text{H}]_i | z_i, \sigma_i, k, b)$ for $[\text{Fe}/\text{H}]_i$ is

$$P([\text{Fe}/\text{H}]_i | z_i, \sigma_i, k, b) = \frac{1}{\sqrt{2\pi}\sigma_i} \exp\left(-\frac{([\text{Fe}/\text{H}]_i - kz_i - b)^2}{2\sigma_i^2}\right) \quad (10)$$

the likelihood L is

$$L = \prod_{i=1}^N P([\text{Fe}/\text{H}]_i | z_i, \sigma_i, k, b). \quad (11)$$

We aim to derive the parameter value (k, b) that maximizes the likelihood function. Here, we use the Bayesian approach to derive the uncertainty of the metallicity vertical gradient. The metallicity vertical gradient of the HVTD is $d[\text{Fe}/\text{H}]/dz = -0.11 \pm 0.0004 \text{ dex/kpc}$ as shown in the Figure 4 bottom left panel. The HVTD is mainly distributed in

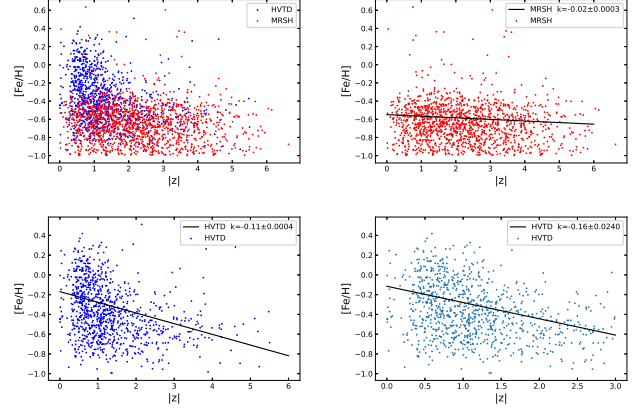


FIG. 4.— Top left panel: Metallicity distribution as function of $|z|$ (kpc) for HVTD marked by the blue dots and MRSH marked by the red dots. The distribution of HVTD is relatively concentrated, and the distribution of MRSH is relatively uniform. Top right panel: Metallicity distribution as function of $|z|$ of MRSH, $d[\text{Fe}/\text{H}]/dz = -0.02 \pm 0.0003 \text{ dex/kpc}$. Bottom left panel: Metallicity distribution as function of $|z|$ for the HVTD, $d[\text{Fe}/\text{H}]/dz = -0.11 \pm 0.0004 \text{ dex/kpc}$. Bottom right panel: Metallicity distribution as function of $|z|$ for the HVTD in the range $|z| < 3 \text{ kpc}$, $d[\text{Fe}/\text{H}]/dz = -0.16 \pm 0.0008 \text{ dex/kpc}$.

$z < 3 \text{ kpc}$, we calculated the metallicity vertical gradient in this range, $d[\text{Fe}/\text{H}]/dz = -0.16 \pm 0.0008 \text{ dex/kpc}$.

This result is roughly consistent with some previous result of the thick disk. For example, Chen et al. (2011) used RHB stars with range in $0.5 - 3 \text{ kpc}$ to give the gradient for the thick disk $d[\text{Fe}/\text{H}]/dz = -0.12 \pm 0.01 \text{ dex/kpc}$. Bilir et al. (2012) used red clump stars to derive that the vertical metallicity gradient for the thick disk is close to zero. Mikolaitis et al. (2014) given $d[\text{Fe}/\text{H}]/dz = -0.072 \pm 0.006 \text{ dex/kpc}$. Li & Zhao (2017) given the result $d[\text{Fe}/\text{H}]/dz = -0.164 \pm 0.010 \text{ dex/kpc}$. Tunçel Güçtekin et al. (2019) reported $d[\text{Fe}/\text{H}]/dz = -0.164 \pm 0.014 \text{ dex/kpc}$ with range $6 < R < 10 \text{ dex/kpc}$ and $2 < |z| < 5 \text{ dex/kpc}$. Yan et al. (2019) reported $d[\text{Fe}/\text{H}]/dz = -0.074 \pm 0.0009 \text{ dex/kpc}$ for the thick disk. According to these studies, the gradient of our HVTD sample is very similar to the thick disk, which implies the HVTD sample have very obvious characteristics of the thick disk.

In the top right plane of Figure 4, the metallicity vertical gradient of the MRSH is $d[\text{Fe}/\text{H}]/dz = -0.02 \pm 0.0003 \text{ dex/kpc}$, which is a very flat gradient. This result is roughly consistent with previous results of halo, Tunçel Güçtekin et al. (2019) given the vertical metallicity gradients $d[\text{Fe}/\text{H}]/dz = -0.023 \pm 0.006 \text{ dex/kpc}$ in the interval $6 < R < 10 \text{ kpc}$. Peng et al. (2012, 2013) derived that the vertical gradient $d[\text{Fe}/\text{H}]/dz = -0.05 \pm 0.04 \text{ dex/kpc}$ and $d[\text{Fe}/\text{H}]/dz = -0.03 \pm 0.02 \text{ dex/kpc}$ for distance $5 < z \leq 14 \text{ kpc}$ and they concluded that there is little or no gradient in the halo. Other studies also given the gradient closed to zero at larger galactocentric distances for the halo.

3. THE CHEMICAL ELEMENTS ABUNDANCE ANALYSIS

3.1. Stellar Elements Abundance distribution

APOGEE DR16 provides a large number of chemical elements abundance of stars. Jönsson et al. (2020) points out some parameters are not accurate enough and should be selected according to the effective temperature. We selected 11 elements and α -element as a function of $[\text{Fe}/\text{H}]$ to study the chemical properties and origins of sample stars. These ele-

ments abundance distributions are given in Figure 5. We also derived the important parameter $[\alpha/\text{Fe}]$, where α refers to the average abundance of Mg, Si, Ca, Ti. The α -elements are often used as an indicator of time scale in studying the history of star formation. This is mainly due to the α -elements produced in type II supernovae explosion on a relatively short time scale (10^7 years). While iron is produced on a much longer time scale (10^9 years) by type Ia supernovae explosion. So the analysis of the α -elements is particularly important.

C, N and O abundance are also important for probing the star formation history. For example, Masseron & Gilmore (2015) used the variations of carbon and nitrogen abundances of stars in the thin disk and thick disk of the Galaxy to gather information on the relative ages of stars. Martig et al. (2016) used carbon and nitrogen to infer the mass of the stars. Although the derived ages are with rms errors of 40 percent, these element abundance is still important to study the formation history.

As shown in each panel of Figure 5, there are a large number of overlapping areas in these distributions. In areas with rich metallicity, most sample stars belong to the HVTd. The MRSH sample stars are mainly distributed in the range with $[\text{Fe}/\text{H}] < -0.2$ dex. In addition, from the distribution in the $[\text{X}/\text{Fe}]$ vs. $[\text{Fe}/\text{H}]$ (X refers the selected elements), we noticed that some chemical elements display centralized distribution, like N, Ca, Si, Mn for the HVTd and MRSH, as well C, Al, Co for the HVTd, but some elements appear scattered distribution, like O, Mg, Ti, Ni for the HVTd and MRSH.

3.2. Data Dimensionality Reduction

We selected 11 elements (C, N, O, Mg, Al, Si, Ca, Ti, Mn, Co, Ni) which are accurate in APOGEE DR16. These elements with $[\text{Fe}/\text{H}]$ constitute a high-dimensional data space, and comprehensive understanding and interpreting of multi-dimensional abundance distribution is not easy. We try to reduce dimensionality of multi-dimensional data. The common data dimensionality reduction method is principal component analysis (PCA) algorithm, which is a linear algorithm. But the results of this algorithm are not reliable when the data has complex connections. So for highly-correlated datasets (like chemical-abundance distribution in this work), non-linear dimensionality reduction processing algorithm is necessary.

Here, we use t-distributed stochastic neighbor embedding method (t-SNE; Van der Maaten & Hinton 2008) which is a non-linear machine-learning algorithm, and it can reduce N-dimensional data to a 2D plane. In this work, each star has 11 elements abundances and metallicity $[\text{Fe}/\text{H}]$. These elements constitute a high-dimensional data space (Fe, C, N, O, Mg, Al, Si, Ca, Ti, Mn, Co, Ni), each element is a dimension. The t-SNE algorithm can reduce each sample star with 12-dimensional data characteristics to two dimensions and represent it with a set of coordinates, and use a set of two-dimensional plane coordinates to make the results easier to visualize. Data points (stars) with similar characteristics on this plane will gather together.

The principle of the algorithm is: given a N high-dimensional data points $\mathbf{x}_1, \dots, \mathbf{x}_N$ (here represent abundances), t-SNE first computes probabilities p_{ij} that are proportional to the similarity of objects \mathbf{x}_i and \mathbf{x}_j , as follows:

$$p_{ji} = \frac{\exp(-\|\mathbf{x}_i - \mathbf{x}_j\|^2/2\sigma_i^2)}{\sum_{i \neq k} \exp(-\|\mathbf{x}_i - \mathbf{x}_k\|^2/2\sigma_i^2)}, \quad (12)$$

and define symmetrized similarity :

$$p_{ij} = \frac{p_{ji} + p_{ij}}{2N}. \quad (13)$$

t-SNE aims to learn a d-dimensional map $\mathbf{y}_1, \dots, \mathbf{y}_N$ (with $\mathbf{y}_i \in \mathbb{R}^d$) that reflects the similarities p_{ij} as well as possible.

For the low-dimensional counterparts \mathbf{y}_i and \mathbf{y}_j of the high-dimensional data points \mathbf{x}_i and \mathbf{x}_j , it is possible to compute a similar conditional probability, which is denoted by q_{ji} . It reflects the similarities between two points \mathbf{y}_i and \mathbf{y}_j in the low-dimensional map. For the low-dimensional, we choose the variance of the Gaussian to $1/\sqrt{2}$

$$q_{ji} = \frac{\exp(-\|\mathbf{y}_i - \mathbf{y}_j\|^2)}{\sum_{i \neq k} \exp(-\|\mathbf{y}_i - \mathbf{y}_k\|^2)}. \quad (14)$$

In the case of symmetry,

$$q_{ij} = \frac{\exp(-\|\mathbf{y}_i - \mathbf{y}_j\|^2)}{\sum_{k \neq l} \exp(-\|\mathbf{y}_k - \mathbf{y}_l\|^2)}. \quad (15)$$

In t-SNE algorithm, we employ a Student t-distribution with one degree of freedom as the heavy-tailed distribution in the low-dimensional map. Using this distribution, the joint probabilities q_{ij} are defined as

$$q_{ij} = \frac{(1 + \|\mathbf{y}_i - \mathbf{y}_j\|^2)^{-1}}{\sum_{k \neq l} (1 + \|\mathbf{y}_k - \mathbf{y}_l\|^2)^{-1}}. \quad (16)$$

The locations of the points \mathbf{y}_i in the map are determined by minimizing the (non-symmetric) Kullback-Leibler divergence of the distribution P from the distribution Q , that is:

$$KL(P||Q) = \sum_{i \neq j} p_{ij} \log \frac{p_{ij}}{q_{ij}}. \quad (17)$$

The minimization of the Kullback-Leibler divergence is performed by using gradient descent. The result of this optimization is a 2D plane that reflects the similarities between the high-dimensional data points (Van der Maaten & Hinton 2008).

We use scikit-learn (Pedregosa et al. 2011) packages in python to implement this algorithm. The method has one main parameter perplexity, p , which governs the bandwidth of the Gaussian kernels σ_i and appears in the similarities p_{ij} , in this work we take $p = 50$. Another parameters is learning rate and set to 1, and the early-exaggeration parameter is not important, so we take the default value, and random state in scikit-learn packages is set to 1.

We give the final result of this algorithm in Figure 6, the HVTd sample is marked by blue dots and the MRSH sample is marked by orange dots. At the same time, we have drawn the distribution of different parameters ($[\text{X}/\text{Fe}]$, $[\text{Fe}/\text{H}]$, eccentricity e and vertical distance $|z|$) in Figure 7.

The entire sample is divided into three areas in Figure 6 :

- Area A in HVTd
- Area B in MRSH
- Overlapping area of HVTd and MRSH

Area A and B denote two independent parts in the dimensionality reduction result, which mainly contains HVTd and MRSH, respectively.

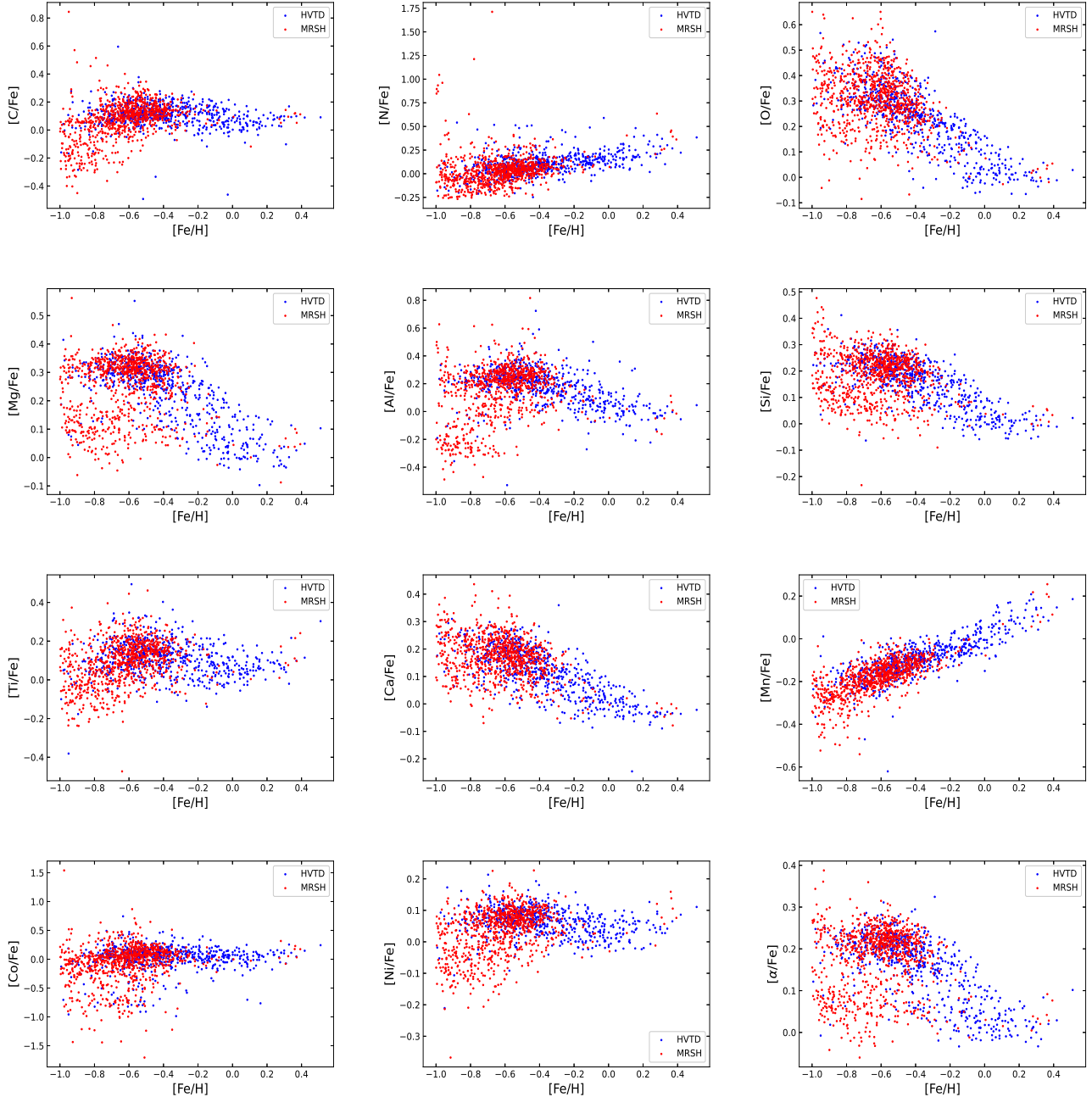


FIG. 5.— Element abundance distribution versus $[\text{Fe}/\text{H}]$. We removed some obvious inaccurate data. The high-velocity thick disk (HVT, marked by the blue dots) and metal-rich stellar halo (MRSH, marked by the red dots).

4. DISCUSSION ABOUT THE ORIGINS OF THE MRSH AND HVT

Some previous works suggested some possible origin about those metal-rich halo stars (e.g., Bonaca et al. 2017; Gallart et al. 2019; Belokurov et al. 2019; Yan et al. 2020). For example, Bonaca et al. (2017) proposed that metal-rich halo stars within 3kpc from the sun may have formed in situ, rather than having been accreted from satellite systems, and these metal-rich halo stars have likely undergone substantial radial migration or heating. Yan et al. (2020) proposed that for the young stars (< 9 Gyr), their formation may not be affected by the Gaia-Sausage merger. The MRSH stars were likely born in-situ rather than accreted from the Gaia-Sausage merger. But for the old stars formed in-situ (> 9 Gyr), the Gaia-Sausage

merger event may have a major effect on their formation. The MRSH stars may form in an old proto-disk, possibly dynamically heated by the Gaia-Sausage merger, and subsequently be kicked out to the halo.

In this study, based on the dimensionality reduction results, we found there are obvious regional chemical characteristics, as shown in Figure 6. The stars in zone B are mainly MRSH, the stellar metallicity in this region lies between -1 dex and -0.6 dex. But it still has lower α -element abundances. The $[\text{Mg}/\text{Fe}]$, $[\text{Al}/\text{Fe}]$, $[\alpha/\text{Fe}]$ here is obviously much smaller than the overlap area. It is very similar to the chemical characteristics of dwarf galaxies. Letarte et al. (2010) showed such element abundance characteristics for field stars of dwarf galaxies (Fornax). Hawkins et al. (2015) also showed

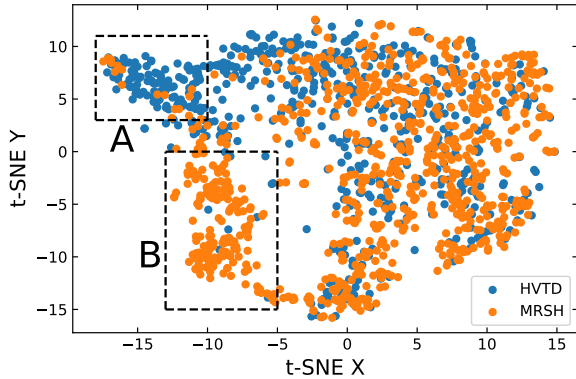


FIG. 6.— Dimensionality reduction result, the HVTD sample is marked by blue dots and the MRSH sample is marked by orange dots. The result contains two parts with a single component (HVTD and MRSH), marked A and B, respectively.

in more details the abundance patterns of the elements as a function of metallicity for the disks stars, halo stars and dwarf galaxy (Fornax), which clearly implied lower α -element with $[\text{Fe}/\text{H}]$ from -1.0 dex to -0.5 dex for dwarf galaxies. Fattahi et al. (2019) revealed the origin of the metal-rich halo stars ($[\text{Fe}/\text{H}] \sim -1$ dex) with highly eccentric orbits (high orbital anisotropy, $\beta > 0.8$), by tracing their stars back to the epoch of accretion and showed these stars could come from a single dwarf galaxy. Those sample stars in area B also have extremely high eccentricities in the last row of the middle column of Figure 7. Therefore, we conclude that those stars in area B for the MRSH are chemically and kinematic consistent with dwarf galaxies.

The overlapping area in the HVTD and MRSH which have same element abundances means that they have similar origin. The possible origin in these regions were in-situ. After undergoing some processes, some stars become halo stars, and other stars still maintain the kinematic characteristics of disk stars. The in-situ population can contain stars formed in the initial gas collapse (Samland & Gerhard 2003). Cooper et al. (2015) gave two distinct origins of in-situ halo stars: gas that has been stripped from satellite galaxies by tides and ram pressure, and gas is incorporated directly into the smooth halo of the main galaxy by cosmological infall and Supernova-Driven outflow from the central galaxy.

In addition, the overlapping area could also include some stars originated from within the Milky Way disk. Bonaca et al. (2017) proposed two disk heating mechanisms to form the metal-rich halo stars: runaway stars and radial migration. Runaway stars are young stars that are formed in the disk and then ejected from their birthplace. Based on the discussion of metallicity and spectral type in Bonaca et al. (2017), combined with the characteristics of our sample, we can conclude that runaway stars are a minor component of the observed metal-rich stellar halo.

Radial migration has been recognized as a important component in explaining numerous observations such as the spread in the age-metallicity relation (e.g., Sellwood & Binney 2002; Roškar et al. 2008; Minchev & Famaey 2010) and its abundance patterns (Schöenrich & Binney 2009a). El-Badry et al. (2016) proposed star experienced significant radial migration by two related processes. First, some stars are formed during gas outflows, so that their initial orbits can be eccentric and have large apocenters. Second, the gravitational

potential of the galaxy will have strong fluctuations under the combination of the inflow gas accretion and gas outflow. This fluctuation will affect the stellar orbits, which will eventually become heated to a more isotropic distribution. Because those stars within the overlapping area have similar chemical compositions and orbital eccentricities, it indicates that they have the same origin and may have undergone similar processes. We consider radial migration is an possible formation mechanism for the stars in the overlapping area.

For the stars in the area A, as we shown in Figure 7, their characteristics are very obvious (e.g. high $[\text{Fe}/\text{H}]$, low eccentricity, low α -element). The stars in area A are mainly HVTD, the stellar metallicity in this region lies between -0.2 dex and 0.4 dex. These stars in this region have the characteristics of thin disk stars. According to the proposed formation mechanism of thick disk, we infer that these stars could originate from the heating of a pre-existing thin disk.

The stellar ages also provide important clues to probe the possible origins of the population. But it is difficult to obtain the accurate ages of stars. Here, we use the age range of the stars to discuss the potential origins of the MRSH and HVTD. Ages of our sample stars are obtained by cross-matching with catalog of Sanders18 catalog (Sanders & Das 2018). Sanders & Das (2018) only estimated masses and ages for the stars metal-richer than -1.5 dex and the maximum age isochrone considered is 12.6 Gyr. The age distributions in the MRSH and HVTD are shown in Figure 8, which imply that both MRSH and HVTD contain young stars (< 9 Gyr) and old stars (> 9 Gyr). The young MRSH stars were possible born in-situ, but the Gaia-Sausage merger event may have an important effect on the old stars. The HVTD stars also form in an old proto-disk, but these stars may be so less affected by the Gaia-Sausage merger event than MRSH that they remain some properties of the thick disk (Yan et al. 2020).

According to above analysis of chemical element abundance and kinematics and age, we consider that the HVTD and the MRSH each have two origins. The MRSH stars are formed from the accretion of smaller galaxies and in-situ formation. The HVTD stars could originate from the heating of a pre-existing thin disk and in-situ formation.

5. SUMMARY AND CONCLUSIONS

Based on the data of APOGEE DR16 and Gaia DR2, we first obtained high-velocity sample stars ($v_{\text{tot}} \geq 220 \text{ km s}^{-1}$). According to the distribution of rotational velocity and metallicity ($[\text{Fe}/\text{H}] > -1$ dex) of this sample stars, we divide this sample stars into HVTD ($v_{\phi} > 90 \text{ km s}^{-1}$) and MRSH ($v_{\phi} < 90 \text{ km s}^{-1}$) and studied their elements abundance distribution to confirm their origins.

We found the MRSH has relatively low metallicity (-1.0 dex, -0.4 dex), but the HVTD not only has a relatively small number in the lower metallicity $[\text{Fe}/\text{H}]$, but also has more metal-rich stars in metallicity $[\text{Fe}/\text{H}]$ (-0.4 dex, 0.4 dex). Furthermore, we use maximum likelihood method to estimate the vertical metallicity gradient of two samples. The metallicity vertical gradient of the HVTD is $d[\text{Fe}/\text{H}]/d|z| = -0.16 \pm 0.0008 \text{ dex/kpc}$ in $z < 3 \text{ kpc}$, and the metallicity vertical gradient of the MRSH is $d[\text{Fe}/\text{H}]/d|z| = -0.02 \pm 0.0003 \text{ dex/kpc}$, which is a very flat gradient.

The elements abundance of stars can provide important clues to probe their origin. In this study, we selected 11 elements and α -element as a function of $[\text{Fe}/\text{H}]$ to study the chemical properties and origins of sample stars. In order to comprehensively consider various element abundance indica-

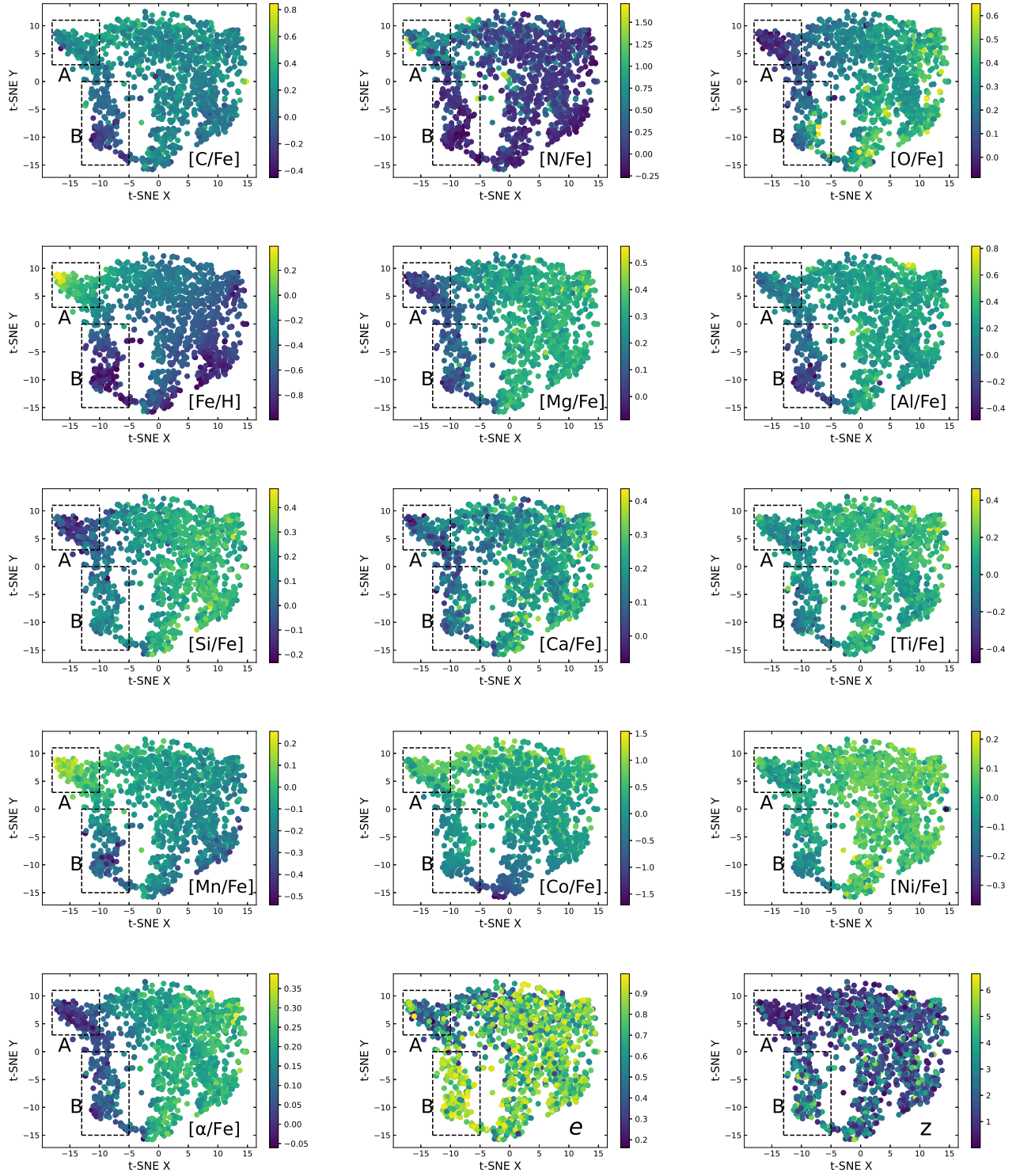


Fig. 7.— t-SNE result, color-coded by chemical abundance, eccentricity e and vertical distance $|z|$. We only used [Fe/H] and [X/Fe] ratios to get t-SNE result.

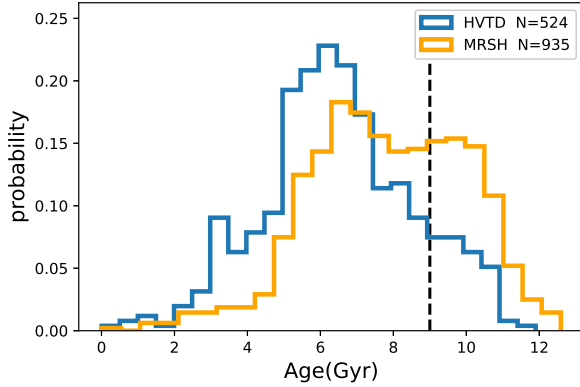


FIG. 8.— Age distributions of the MRSH and HVTD, we get through cross-matching our sample and Sanders & Das (2018). We got 524 HVTD samples with blue lines and 935 MRSH samples with orange lines. The dash line position is 9 Gyr, Samples larger than 9 Gyr have experienced the Gaia–Sausage event as discussion in Yan et al. (2020).

tors, we performed dimensionality reduction processing on the data according to the t-SNE algorithm. It is clear that the sample is divided into three areas: area A in HVTD, area B in MRSH and overlapping area of HVTD and MRSH, which can relate with some formation mechanisms. From the chemical element abundance and kinematics and age, we can conclude that the HVTD and the MRSH each have two origins. The MRSH stars are formed from the accretion of smaller galaxies and in-situ formation. The HVTD stars could originate from the heating of a pre-existing thin disk and in-situ formation.

6. ACKNOWLEDGEMENTS

We thank especially the referee for insightful comments and suggestions, which has improved the paper significantly. This work was supported by the National Natural Foundation of China (NSFC No. 11973042, No. 11973052 and No. 11873053). It was also supported by the Fundamental Research Funds for the Central Universities and the National Key R&D Program of China No. 2019YFA0405501. H.J.N.

REFERENCES

- Abadi M. G., Navarro J. F., Steinmetz M., & Eke V. R., 2003, *ApJ*, 597, 21.
 An D., Beers T. C., Johnson J. A., Pinsonneault M. H., et al., 2013, *ApJ*, 763, 65
 An D., Beers T. C., Santucci R. M., Carollo D., et al., 2015, *ApJL*, 813, L28
 Astraatmadja T. L., & Bailer-Jones C. A. L., 2016a, *ApJ*, 832, 137
 Astraatmadja T. L., & Bailer-Jones C. A. L., 2016b, *ApJ*, 833, 119
 Astropy Collaboration, Price-Whelan, A. M., Sipócz, B. M., et al. 2018, *AJ*, 156, 123
 Astropy Collaboration, Robitaille T. P., Tollerud E. J., et al. 2013, *A&A*, 558, A33
 Bailer-Jones, C. A. L., 2015, *PASP*, 127, 994
 Bailer-Jones C. A. L., Rybizki J., Fouvésneau M., Mantelet G., Andrae R., 2018, *AJ*, 156, 58
 Beers T. C., Carollo D., Ivezić Ž., An D., et al., 2012, *ApJ*, 746, 34
 Beers T. C., Drilling J. S., Rossi S., Chiba M., et al., 2002, *AJ*, 124, 931
 Beers T. C., Norris J. E., Placco V. M., Lee Y. S., et al., 2014, *ApJ*, 794, 58
 Beers T. C., Sommerlarsen J., 1995, *ApJS*, 96, 175
 Belokurov V., Erkal D., Evans N. W., Koposov S. E., & Deason A. J. 2018, *MNRAS*, 478, 611
 Belokurov V., Sanders J. L., Fattahi A., Smith M. C., et al., 2019 *arXiv:1909.04679*
 Belokurov, V., Sanders, J. L., Fattahi, A., et al., 2020, *MNRAS*, doi:10.1093/mnras/staa876
 Bensby T., Feltzing S., Lundström I., Ilyin I., 2005, *A&A*, 433, 185
 Bergemann M., Collet R., Schönrich R., Andrae R., et al., 2017, *ApJ*, 847, 16
 Bilir S., Karaali S., Ak S., et al., 2012, *MNRAS*, 421, 3362
 Bird S. A., Xue X.X., Liu C., et al., 2020, *arXiv:2005.05980*
 Bland-Hawthorn J., Gerhard O., 2016, *ARA&A*, 54, 529
 Bonaca A., Conroy C., Wetzel A., Hopkins P. F., et al., 2017, *ApJ*, 845, 101
 Bonaca, A., Conroy, C., Cargile, P. A., et al. 2020, *arXiv e-prints*, arXiv:2004.11384
 Bovy J., 2015, *ApJS*, 216, 29
 Brook C. B., Kawata D., Gibson B. K., Freeman K. C., 2004, *ApJ*, 612, 894
 Carollo D., Beers T. C., Lee Y. S., Chiba M., et al., 2007, *Nature*, 450, 1020
 Carollo D., Beers T. C., Chiba M., Norris J. E., et al., 2010, *ApJ*, 712, 692
 Carollo D., Beers T. C., Bovy J., et al., 2012, *ApJ*, 744, 195
 Carollo D., Chiba M., Ishigaki M., Freeman K., et al., 2019, *ApJ*, 887, 22
 Carollo D., Chiba M., 2020, *arXiv 2010.00235v1*
 Chen Y. Q., Zhao G., Carrell K., & Zhao J. K. 2011, *ApJ*, 142, 184
 Chiba M., Beers T. C., 2000, *AJ*, 119, 2843
 Cooper A. P., Parry O. H., Lowing B., Cole S., et al., 2015, *MNRAS*, 454, 3185
 Conroy C., Naidu R. P., Zaritsky D., et al., 2019, *ApJ*, 887, 237
 Deason A. J., Belokurov V., Koposov S. E., Lancaster L., 2018, *ApJL*, 862, L1
 Eisenstein, D. J., Weinberg, D. H., Agol, E., et al. 2011, *AJ*, 142, 72
 El-Badry K., Wetzel A., Geha M., et al. 2016, *ApJ*, 820, 131

acknowledges funding from US NSF grant AST-1908653. This project was developed in part at the 2016 NYC Gaia Sprint, hosted by the Center for Computational Astrophysics at the Simons Foundation in New York City.

Funding for the Sloan Digital Sky Survey IV has been provided by the Alfred P. Sloan Foundation, the U.S. Department of Energy Office of Science, and the Participating Institutions. SDSS-IV acknowledges support and resources from the Center for High-Performance Computing at the University of Utah. The SDSS web site is www.sdss.org.

SDSS-IV is managed by the Astrophysical Research Consortium for the Participating Institutions of the SDSS Collaboration including the Brazilian Participation Group, the Carnegie Institution for Science, Carnegie Mellon University, the Chilean Participation Group, the French Participation Group, Harvard-Smithsonian Center for Astrophysics, Instituto de Astrofísica de Canarias, Johns Hopkins University, Kavli Institute for the Physics and Mathematics of the Universe (IPMU) / University of Tokyo, Lawrence Berkeley National Laboratory, Leibniz Institut für Astrophysik Potsdam (AIP), Max-Planck-Institut für Astronomie (MPIA Heidelberg), Max-Planck-Institut für Astrophysik (MPA Garching), Max-Planck-Institut für Extraterrestrische Physik (MPE), National Astronomical Observatories of China, New Mexico State University, New York University, University of Notre Dame, Observatório Nacional / MCTI, The Ohio State University, Pennsylvania State University, Shanghai Astronomical Observatory, United Kingdom Participation Group, Universidad Nacional Autónoma de México, University of Arizona, University of Colorado Boulder, University of Oxford, University of Portsmouth, University of Utah, University of Virginia, University of Washington, University of Wisconsin, Vanderbilt University, and Yale University.

This work has made use of data from the European Space Agency (ESA) mission Gaia (<http://www.cosmos.esa.int/gaia>), processed by the Gaia Data Processing and Analysis Consortium (DPAC, <http://www.cosmos.esa.int/web/gaia/dpac/consortium>). Funding for DPAC has been provided by national institutions, in particular the institutions participating in the Gaia Multilateral Agreement.

- Fattahi A., Belokurov V., Deason A. J., et al. 2019, MNRAS, 484, 4471
 Feuillet, D. K., Frankel, N., Lind, K., et al. 2019, MNRAS, 489, 1742
 Foreman-Mackey, D., Hogg, D. W., Lang, D., & Goodman, J. 2013, PASP, 125, 306
 Gaia Collaboration, Brown A. G. A., Vallenari A., et al., 2018a, A&A, 616, A1
 Gaia Collaboration, Katz D., Antoja T., et al., 2018b, A&A, 616, A11
 Gallart C., Bernard E. J., Brook C. B., Ruiz-Lara T., et al., 2019
 arXiv:1901.02900
 Gandhi, S. S., Ness, M. K., 2019, ApJ, 880,134
 Grand, R. J. J., Kawata, D., Belokurov, V., et al. 2020, MNRAS, 497, 1603
 Gu J. Y., Du C. H., Jia Y. P., Peng X. Y., et al., 2015, MNRAS, 452, 3092
 Gu J. Y., Du C. H., Jing Y. J., Zuo W. B., 2016, ApJ, 826, 36
 Gu J. Y., Du C. H., Zuo W. B., 2019, ApJ, 877, 83
 Han D. R., Lee Y. S., Kim Y. K., Beers T. C., 2020, ApJ, 896, 14
 Hawkins K., Kordopatis G., Gilmore G., et al. 2015, MNRAS, 447, 2046
 Haywood M., Di Matteo P., Lehnert M. D., Snaith O., et al., 2018, ApJ, 863, 113
 Hayes C. R., Majewski S. R., Hasselquist S., et al., 2018, ApJ, 859, 8
 Helmi A., Babusiaux C., Koppelman H. H., Massari D., et al., 2018, Nature, 563, 85
 Ivezić Ž., Beers T. C., Jurić M., 2012, ARA&A, 50, 251
 Jing Y. J., Du C. H., Gu J. Y., Jia Y. P., et al., 2016, MNRAS, 463, 3390
 Jönsson, H., Holtzman, J. A., Allende Prieto, C., et al., 2020, AJ, submitted
 Kinman T. D., Cacciari C., Bragaglia A., Smart R., et al., 2012, MNRAS, 422, 2116
 Koppelman H. H., Helmi A., Massari D., et al., 2019, A&A, 631, 9
 Kordopatis G., Recio-Blanco A., Schultheis M., et al., 2020, A&A, 643, A69
 van der Kruit P. C., Freeman K.C., 2011, ARA&A, 49, 301
 Lancaster L., Kopusov S. E., Belokurov V., Evans N. W., et al., 2019, MNRAS, 486, 378
 Letarte B., Hill V., Tolstoy E., et al., 2010, A&A, 523, 17
 Li C. D., Zhao G., 2017, ApJ, 850, 25
 Liu C., & van de Ven, G., 2012, MNRAS, 425(3), 2144.
 Liu S., Du C. H., Newberg H. J., Chen Y. Q., et al., 2018, ApJ, 862, 163
 Luri X., Brown A. G. A., Sarro L. M., et al., 2018, A&A, 616, A9
 Martig M., Foesneau M., Rix H.-W., et al., 2016, MNRAS, 456, 3655
 Masseron T., & Gilmore G., 2015, MNRAS, 453(2), 1855.
 McMillan P. J., 2017, MNRAS, 465, 76
 Myeong G. C., Evans N. W., Belokurov V., Sanders J. L., et al., 2018, ApJL, 863, L28
 Myeong G. C., Vasiliev E., Iorio G., Evans N. W., et al., 2019, MNRAS, 488, 1235
 Mikolaitis Š., Hill V., Recio-Blanco A., et al., 2014, A&A, 572, A33
 Minchev I., & Famaey B. 2010, ApJ, 722, 112
 Morrison H. L., Flynn C., Freeman K. C., 1990, AJ, 100, 1191
 Naidu R. P., Conroy C., Bonaca A., et al., 2020, ApJ, 901,48
 Nissen P. E., Schuster W. J., 2010, A&A, 511, L10
 Nissen P. E., Schuster W. J., 2011, A&A, 530, A15
 Pedregosa, F., Varoquaux, G., Gramfort, A., et al. 2011, J. Mach. Learn. Res., 12, 2825
 Posti L., Helmi A., Veljanoski J., Breddels M. A., 2018, A&A, 615, A70
 Peng X.Y., Du C.H., Wu Z.Y., 2012, MNRAS, 422, 2756
 Peng X.Y., Du C.H., Wu Z.Y., et al., 2013, MNRAS, 434, 3165
 Peng X.Y., Wu Z.Y., Qi Z.X., et al., 2018, PASP, 130, 4102
 Prochaska J. X., Naumov S. O., Carney B. W., McWilliam A., Wolfe A. M., 2000, AJ, 120, 2513
 Quinn, P. J., Hernquist, L., & Fullagar, D. P. 1993, ApJ, 403, 74
 Roškar R., Debattista V. P., Quinn T. R., Stinson G. S., & Wadsley J. 2008, ApJL, 684, L79
 Şahin T., Bilir S., 2020, ApJ, 899,411
 Sales L. V., Helmi A., Abadi M. G., et al. 2009, MNRAS, 400, 61
 Samland M., Gerhard O. E., 2003, A&A, 399, 961
 Sanders J. L., Das P., 2018, MNRAS, 481, 4093
 Sellwood J. A., & Binney J. J., 2002, MNRAS, 336, 785
 Schönrich R., & Binney J. J., 2009, MNRAS, 396, 203
 Schönrich R., & Binney J.J., 2009, MNRAS, 399,1145
 Schönrich R., Asplund M., Casagrande L., 2011, MNRAS 415, 3807
 Steinmetz M., Zwitter T., Siebert A., et al. 2006, AJ, 132, 1645
 Tunçel Güçtekin, S., Bilir, S., Karaali, S., et al., 2019, AdSpR, 63, 1360
 Van der Maaten, L., & Hinton, G., 2008, The Journal of Machine Learning Research, 9, 85
 Villalobos Á., Helmi A., 2008, MNRAS, 391(4), 1806
 Wu Y. Q., Xiang M.S., Chen Y.Q., et al., 2021, MNRAS, 501, 4917
 Xiang M.S., Liu X.W., Yuan H.B., et al., 2015, Res. Astron. Astrophys., 15, 1209
 Xiang M.S., Liu X.W., Shi J.R., et al., 2017, ApJS, 232, 2
 Yan Y. P., Du C. H., et al., 2020, ApJ, 903, 131
 Yan Y. P., Du C. H., et al., 2019, ApJ, 880, 36
 Yuan Z., Myeong G.C., Beers T., et al., 2020, ApJ, 891, 39
 Zasowski G., Johnson J. A., Frinchaboy P. M., Majewski S. R., et al., 2013, AJ, 146, 81
 Zhao G., Zhao Y. H., Chu Y. Q., Jing Y. P., et al. 2012, RAA, 12, 723
 Zuo W., Du C. H., Jing Y. J., Gu J. Y., et al., 2017, ApJ, 841, 59